Applied Mathematical Modelling 97 (2021) 463–482

Contents lists available at ScienceDirect

Applied Mathematical Modelling

journal homepage: www.elsevier.com/locate/apm

Non-Newtonian phase change study of nano-enhanced n-octadecane comprising mesoporous silica in a porous medium

S.A.M. Mehryan[a], Mohammad Ghalambaz[b,c,*], Mohammad Vaezi[d], Seyed Mohsen Hashem Zadeh[e], Nima Sedaghatizadeh[f], Obai Younis[g,h], Ali J. Chamkha[i,j], Hani Abulkhair[j,k]

[a] Young Researchers and Elite Club, Yasooj Branch, Islamic Azad University, Yasooj, Iran
[b] Metamaterials for Mechanical, Biomechanical and Multiphysical Applications Research Group, Ton Duc Thang University, Ho Chi Minh City, Vietnam
[c] Faculty of Applied Sciences, Ton Duc Thang University, Ho Chi Minh City, Vietnam
[d] Faculty of mechanical engineering, K. N. Toosi University of Technology, Tehran, Iran
[e] Department of Mechanical Engineering, Shahid Chamran University of Ahvaz, Ahvaz, Iran
[f] School of Mechanical Engineering, The University of Adelaide, Australia
[g] Department of Mechanical Engineering, College of Engineering at Wadi Addwaser, Prince Sattam Bin Abdulaziz University, KSA
[h] Department of Mechanical Engineering, Faculty of Engineering, University of Khartoum, Sudan
[i] Faculty of Engineering, Kuwait College of Science and Technology, Doha Area, Kuwait
[j] Center of Excellence in Desalination Technology, King Abdulaziz University, P.O. Box 80200, Jeddah, 21589, Saudi Arabia
[k] Mechanical Engineering Department, King Abdulaziz University, P.O. Box 80204, Jeddah, 21589, Saudi Arabia

ARTICLE INFO

Article history:
Received 22 November 2020
Revised 19 February 2021
Accepted 16 March 2021
Available online 26 March 2021

Keywords:
Nano-enhanced phase change material (NePCM)
Non-Newtonian molten liquid
Phase-change heat transfer
Porous medium

ABSTRACT

Poor thermal conductivity of phase change materials (PCMs) is the principal barrier to their widespread application. As such, numerous single or hybrid techniques have been proposed to lower the thermal resistance of PCMs. In the present paper, a hybrid approach, including the dispersing of nano-sized particles and embedding in a porous medium, was employed to augment the rate of heat transfer and melting process of the resulting nano-enhanced PCM (NePCM). Aluminum foam was used as the solid matrix, and phase-change heat transfer of a NePCM comprising n-octadecane as the phase change substance and nano-sized particles of mesoporous silica ($MPSiO_2$) was studied. Previous experimental studies have shown that, although n-octadecane behaves as a Newtonian fluid, the mentioned NePCM behavior deviates from that of Newtonian fluids. Hence, the thermal and hydrodynamic behaviors of the non-Newtonian suspension of the NePCM in porous media were investigated numerically. Governing equations, including mass and momentum conservation for the liquid NePCM and energy equations for both solid and liquid phases, were solved using the Galerkin finite element method. The deformed mesh technique was employed to address the movement of the melting front. The finite element code was validated against several experimental and numerical works and was sufficiently accurate. Results showed that owing to the alteration of the rheological and thermophysical characteristics of the NePCM, increasing concentration of nanoparticles reduced the average Nusselt number and the normalized melt volume fraction (*NMVF*). It was also found that porosity played an important role in the phase-change rate. Although the steady-state condition

* Corresponding author.
E-mail addresses: mohammad.ghalambaz@tdtu.edu.vn (M. Ghalambaz), a.chamkha@kcst.edu.kw (A.J. Chamkha), haboalkhair@kau.edu.sa (H. Abulkhair).

https://doi.org/10.1016/j.apm.2021.03.029

was achieved faster in the case of lowest porosity, the maximum *NMVF* was achieved in the case of the highest porosity after Fourier number = 0.02.

1. Introduction

Effective management of the energy produced from renewable resources by utilizing efficient energy storage, consumption control, and recycling the wastage are the key contributors to a sustainable energy plan [1,2]. The intermittency and discontinuous nature of these sources demand efficient energy storage systems [3]. There is hardly a machine or device in which heat transfer does not occur and does not affect its performance, thus improving the thermal performance of devices is vital for technological advancement and lowering energy consumption [4]. A noticeable approach to improve thermal performance and lowering the net energy consumption is to improve the heat transfer rate while recovering wasted thermal energy.

Since their introduction, phase change materials (PCMs) have been extensively employed to store thermal energy via latent heat, especially at low temperatures [1]. Their high heat capacity and small temperature variation during the capturing and releasing of energy make them suitable for a wide range of applications such as heat pumps, smart temperature adaptable textiles, and heat exchangers [5,6]. However, these materials have low thermal conductivity, which negatively affects the phase-change rate and, consequently, the storing and releasing processes [7]. Several methods have been proposed to improve the thermal conductivity of PCMs based on increasing the heat transfer surface, such as using fins, metal foams, graphite matrix, and dispersion of nanostructured materials [8,9]. Mousavi et al. [10] employed a combination of fins and Al_2O_3 nanoparticles to improve the thermal performance of PCMs in energy storage units. The combination of fins and nano-additives could notably improve the melting time. The nanoparticles can also migrate in a liquid and form concentration gradients [11]. The heat transfer aspects of nanoparticle additives in PCMs and metal foams have been well reviewed [12].

Highly conductive porous foams (mainly copper, aluminum, and nickel foams) have been used as a fascinating option for improving the thermal conductivity of thermal storage systems, and, hence, numerous works can be found in this regard. For instance, Mancin et al. [13] surveyed the phase change of three different paraffin-waxes placed in a porous copper foam. Their results revealed that copper foam substantially enhanced the heat transfer rate. Xiao et al. [14] analyzed the phase change process of composite paraffin, embedded in two different metal foams (nickel and copper foams), in latent heat energy storage. They showed that in comparison to pure PCM, the thermal conductivity of the composite paraffin could be enhanced to about three times for nickel foam and 15 times for copper foam. Heyhat et al. [15] investigated the benefit of using PCMs for thermal management of lithium-ion batteries. They used metal inserts (fins), metal foams, and nanoparticles to enhance the heat transfer performance of PCMs. Using metal foams produced better thermal enhancement compared to fins with the same amount of copper material.

Sweiden et al. [16] numerically studied the effect of using metallic foam and highly conductive fins on the charging–discharging rate. Both methods enhanced the heat storage process by increasing the melting rate while PCM-saturated porous metal accounted for the higher phase-change rate. Moreover, Xu et al. [17] addressed phase-change heat transfer and melting front evaluation of PCMs in metal foams and clear flow regions. The results showed that using a porous medium accelerated the melting process, but also suppressed the free convection because of the porous medium's low permeability. Thus, conduction was the dominant heat transfer mechanism in a porous medium filled with a PCM. The authors concluded that employing metal foams for thermal enhancement of PCMs is a vital practical approach.

The addition of a small amount of highly conductive material is another way to increase heat transfer in a medium [18]. Similar to nanofluids, it is anticipated that addition of highly conductive nano-structures increases the thermal conductivity of the base material. Several types of nanostructured materials such as carbon-based structures, oxide nanoparticles, and metallic nanoparticles have been utilized to improve the thermal conductivity of the base PCM [19,20]. Literature studies show the effectiveness of using nanoparticles for enhancing heat transfer [21,22]. Barhemmati-Rajab and Zhao examined the effect of boron nitride nanoparticles on the thermal characteristics of calcium chloride hexahydrate ($CaCl_2{\cdot}6H_2O$) as PCM. They reported a 71.9% increase in conductivity of the PCM with 0.5% weight of nanoparticles dispersed inside it [23]. Generally, the effect of dispersed particles is highlighted as temperature increases but non-monotonically with respect to the mass fraction of nanoparticles [24]. Carbon-based nanostructured materials can result in higher thermal conductivity compared with oxide and metallic particles. Wang et al. [25] reported up to a 46% increase in thermal conductivity of palmitic acid at 25°C. Various aspects of heat transfer of nanofluids such as the presence of magnetic field effects [26], conjugate heat transfer, flow in metal foams [27], and entropy generation [28] have been addressed recentlyTable 1.

Because PCMs are being used for thermal energy storage, analysis of their heat transfer aspect is a primary task. However, other important design aspects should also be carefully considered in a thermal energy storage design. For example, as discussed by Zahir et al. [29], a liquid PCM can be cooled to a temperature below the phase-change temperature without freezing. Thus, the discharging of a PCM can be delayed to temperatures below freezing. The shrinkage of solid PCMs during the discharge process is another important aspect that could lead to mechanical issues and should be taken into account in

Nomenclature

Latin symbols

C_p $(kJ/kg{\cdot}L)$	constant pressure's specific heat capacity
F (N)	volume force
F	non-dimensional volume force
Fu (K)	fusion temperature
I	unit matrix
$\vec{g}(m/s^2)$	gravity vector
K $(W/m{\cdot}K)$	thermal conductivity
H $(W/m^2{\cdot}K)$	convection heat transfer coefficient
L (m)	height of the coaxial pipe
L_{sf} (J)	latent heat of fusion
m	consistency parameter for viscosity model
n	power-law index of the viscosity model
$NMVF$	normalized melted volume fraction
Nu	Nusselt number
p (Pa)	pressure field
P	dimensionless pressure field
Pr	Prandtl number
T (s)	time
T (K)	temperature field
Fo	Fourier number
Da	Darcy number
Ra	Rayleigh number
Ste	Stefan number

Greek symbols

ρ (kg/m^3)	density
β $(1/K)$	coefficient of thermal expansion
ε	porosity
μ $(Pa{\cdot}s)$	dynamic viscosity
ϕ	nanoparticle's volume fraction
α (m^2/s)	thermal diffusivity
θ	non-dimensional temperature
κ (m^2)	permeability
$\dot{\gamma}(1/s)$	shear rate

Subscripts

avg	averaged property
c	cold wall
eff	effective properties of porous medium
fu	properties at fusion temperature
h	hot wall
i	inner pipe
$LNeP$	liquid state of the nano-enhanced phase change material
LP	liquid state of the pure phase-change material
max	maximum (Eq. 28)
min	minimum (Eq. 18)
na	nano-additives
NeP	nano-enhanced phase change material
o	outer pipe
p	porous medium
$\boldsymbol{r}$	radial direction
SM	solid matrix
$SNeP$	solid state of the nano-enhanced phase change material
w	weight concentration of the nano-additives
$\boldsymbol{z}$	axial direction

design of PCMs [30]. Considering nano-enhanced PCMs (NePCMs), the non-uniformity of nanoparticles in the PCM during the phase-change cycles and segregation and migration of nanoparticles due to thermophoresis and Brownian motion are some aspects that should be considered [31,32].

Although it has been reported that adding nano-additives to the base PCM affects the thermophysical and rheological properties of the PCM, such as its viscosity, few studies have addressed the non-Newtonian behavior of NePCMs [33]. An experimental study by Kumaresan et al. [34] indicated that based on the shear stress, the NePCM could exhibit both shear-thinning and Newtonian behavior. Their results also revealed that viscosity of the NePCM is highly dependent on the volume fraction of the dispersed particles. Generally, experimental studies show that, despite the material of the nanoparticles, a NePCM behaves as a shear-thinning fluid when the mass fraction of the nanoparticles exceeds some critical value. Experimental studies conducted by Motahar et al. [35] show that n-octadecane/TiO_2 behaves as a Newtonian fluid for mass fractions below 2%.

Mesoporous silica ($MPSiO_2$) is an appealing substance for numerous applications due to its porous structure and morphological characteristics [36,37]. Recently, Nikkam et al. [38] dispersed $MPSiO_2$ nanoparticles in a base fluid and studied the rate of heat transfer in the produced nanofluid. The experimental study by Motahar et al. [37] indicated that dispersing $MPSiO_2$ in n-octadecane can affect the rheological properties of liquid PCM, i.e. the power-law index and the intensity coefficient. This study also showed that the viscosity of liquid NePCM with 5 wt.% $MPSiO_2$ is 60% more than that of the pure PCM at 35°C. Mehryan et al. [39], by employing the thermal and rheological properties presented by Motahar et al. [35], modeled the phase-change process of NePCMs containing $MPSiO_2$ nano-additives. They found that dispersing the $MPSiO_2$ nano-additives can lower the rate of phase change. In another investigation, Ghalambaz et al. [40] addressed the non-Newtonian phase-change heat transfer of $MPSiO_2$ NePCMs in an inclined enclosure and found that presence of nano-additives suppressed the free convection heat transfer flows and reduced the melting rate and heat transfer. These authors also discussed that the non-Newtonian flows with phase-change heat transfer are non-linear and complex numerical problems and proposed the deformed mesh approach to handle the phase change non-linearities and eliminate the numerical instabilities due to phase transitions.

As discussed earlier, embedding PCMs in open metal foams is a promising approach to improve the heat transfer and melting rate of PCMs. Because the presence of metal foams limits the free convection flows, in such designs, the conduction heat transfer is the dominant heat transfer mechanism. Thus, using nano-additives could be beneficial as they boost the thermal conductivity of PCMs. Hence, the present work aims to model the phase-change heat transfer of $MPSiO_2$ nano-additives in a metal foam. The presence of these nanoparticles produces non-Newtonian effects in liquid PCM, which will be taken into account. The deformed mesh approach [40] is developed to model and simulate the flow and heat transfer in metal foams.

2. Physical and mathematical model

Fig. 1(a) depicts the three-dimensional view of the differentially heated coaxial pipe utilized in this investigation. The coaxial pipe dimensions were L (height), r_i (inner radius), and r_o (outer radius) in which $L = r_o - r_i$. The inner and outer surfaces of the pipe having T_h and T_c temperatures were thermally active while the upper and lower annuli were considered adiabatic. Since physics was symmetric around the z-axis, the problem could be modeled as a 2D axisymmetric one. The NePCM, consisting of n-octadecane and $MPSiO_2$ nano-additives, was poured into the void spaces of the aluminum foam placed between the inner and outer pipes. The results of Motahar et al. [37] showed that the melted NePCM of n-octadecane and $MPSiO_2$ nano-additives exhibited power-law non-Newtonian behavior. The free convection of the melted NePCM with no volume expansion was simulated using the Boussinesq approximation. In this study, shrinkage was not modeled during the phase-change process. The nano-enhanced/pure PCM properties were considered the average of the properties of solid and liquid phases of the matter. The nano-additive distribution in the n-octadecane was considered to be homogenous. Moreover, it was assumed that there were no thermal and dynamic slips between the dispersed nano-additives and host PCM. Considering these assumptions, a one-fluid mixture model was established to model NePCM behavior.

The mass, momentum, and energy conservation equations, listed below, were employed to simulate the heat transfer and fluid flow of the non-Newtonian NePCM:

$$\bar{\rho}_{NeP}\nabla^* \cdot \vec{u} = 0 \tag{1}$$

$$\frac{\bar{\rho}_{NeP}}{\varepsilon}\frac{\partial \vec{u}}{\partial t} + \frac{\bar{\rho}_{NeP}}{\varepsilon^2}\cdot(\vec{u}\cdot\nabla^*)\vec{u} = \nabla^*\cdot\left[-pI + \mu_{LNeP}\left(\nabla^*\vec{u} + (\nabla^*\vec{u})^{tr}\right)\right] + \vec{f} \tag{2}$$

wherein

$$\mu_{LNeP}(\dot{\gamma}) = m_{LNeP}\dot{\gamma}^{n_{LNeP}-1}\left|\begin{cases}\dot{\gamma} = max\left(\sqrt{[D']:[D']}, \dot{\gamma}_{min}\right)\\ 2D' = \left(\nabla\vec{u} + (\nabla\vec{u})^{tr}\right)\end{cases}\right. \tag{3-a}$$

$$\vec{f} = f_r e_r + f_z e_z \left| f_r = -\frac{\mu_{LNeP}}{\kappa}u_r,\ f_z = -\frac{\mu_{LNeP}}{\kappa}u_z + \bar{\rho}_{NeP}g\beta_{LNeP}\left(T - T_{fu}\right)\right. \tag{3-b}$$

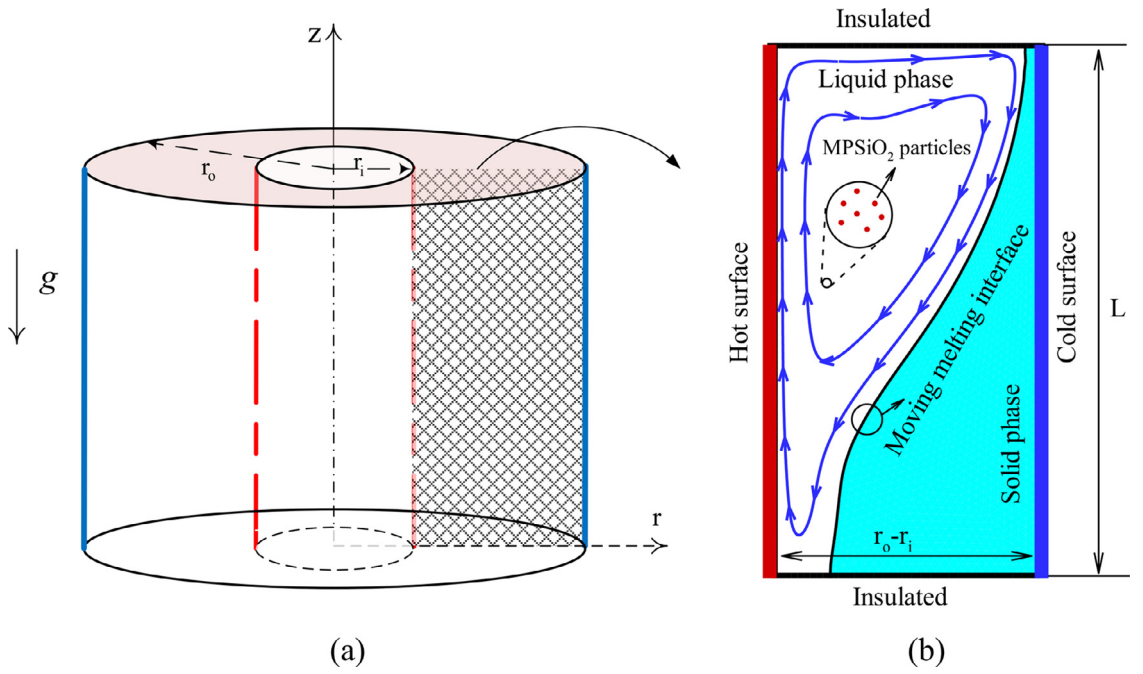

Fig. 1. Schematic view of (a) coaxial pipe and (b) longitudinal section.

In addition, it should be noted that $\bar{\rho}_{NeP}$ is the average density of the NePCM in the liquid and solid phases, as follows:

$$\bar{\rho}_{NeP}=\frac{\rho_{LNeP}+\rho_{SNeP}}{2} \tag{3-c}$$

LNeP and *SNeP*, respectively, denote the liquid and solid phases of the NePCM.

$$(\rho C_p)_{eff,LNeP}\frac{\partial T}{\partial t}+\bar{\rho}_{NeP}C_{p,LNeP}\vec{u}\cdot\nabla^* T=\nabla^*\cdot(k_{eff,LNeP}\nabla^* T) \tag{4}$$

In Eq. (3-a), μ_{LNeP} is the apparent viscosity of the liquid NePCM, which for a power-law non-Newtonian fluid, depends on the shear rate ($\dot{\gamma}$), consistency index (m_{LNeP}), and the power-law index (n_{LNeP}), with *D'* being the strain rate tensor. A fluid is called shear-thinning if $n_{LNeP} < 1$and shear thickening when $n_{LNeP} > 1$. Eq. (3-b) shows the volume forces exerted on the fluid elements, both in *r*- and *z*-directions. The *r*-component and the first term in the *z*-component of the volume forces denote the Darcy term induced by the motion of fluid in the porous medium. The last term in the equation of f_z is the buoyancy force caused by the temperature dependency of the density.

It has been proved that a porous medium can homogenize the distribution of nano-sized particles. The thermophoresis effect, which moves the nanoparticles away from the hot region, is considered the main reason for the non-uniform distribution of nanoparticles. The porous matrix can retard the thermophoresis effect [11]. Hence, single-phase homogeneous models can be accurately employed to address the thermophysical properties of nanofluids in a porous medium. The $(\rho C_p)_{eff,LNeP}$ and $k_{eff,LNeP}$ are the effective volumetric heat capacity and effective thermal conductivity of the liquid NePCM, respectively, and can be calculated as follows:

$$(\rho C_p)_{eff,LNeP}=\varepsilon\bar{\rho}_{NeP}C_{p,LNeP}+(1-\varepsilon)(\rho C_p)_{SM} \tag{5-a}$$

$$k_{eff,LNeP}=\varepsilon k_{LNeP}+(1-\varepsilon)k_{SM} \tag{5-b}$$

$$(\rho C_p)_{eff,SNeP}\frac{\partial T}{\partial t}=\nabla\cdot(k_{eff,SNeP}\nabla T) \tag{6}$$

wherein $(\rho C_p)_{eff,SNeP}$ and $k_{eff,SNeP}$ are defined as:

$$(\rho C_p)_{eff,SNeP}=\varepsilon\bar{\rho}_{NeP}C_{p,SNeP}+(1-\varepsilon)(\rho C_p)_{SM} \tag{7-a}$$

$$k_{eff,SNeP}=\varepsilon k_{SNeP}+(1-\varepsilon)k_{SM} \tag{7-b}$$

Table 1
Thermophysical properties of metal foam [41].

Property [Unit]	Symbol	Value
Thermal conductivity [W/m·K]	k_{SM}	205
Specific heat [J/kg·K]	$C_{p,SM}$	897
Density [kg/m^3]	ρ_{SM}	2700

Table 2
Thermal conductivity and rheological characteristics of the NePCM [37].

Mass fraction of the nano-additives (φ_w) [%]	0.0	0.01	0.03	0.05
Thermal conductivity in liquid phase (k_{LNeP}) [W/m·K]	0.152	0.154	0.157	0.159
Thermal conductivity in solid phase (k_{SNeP}) [W/m·K]	0.371	0.375	0.383	0.380
Power-law index (n)	1	1	0.879	0.822
Consistency (m) [mPa·s^n]	3.536	3.987	7.910	11.021

Table 3
Thermophysical properties of the pure PCM and nano-additives [42,43].

Property	Silica nano-additives	n-Octadecane
Specific heat capacity (solid/liquid) [J/kg·K]	765	1934/2196
Density (solid/liquid) [kg/m^3]	3970	865/770
Latent heat of fusion [kJ/kg]	-	243.5
Thermal expansion coefficient [1/K]	0.63×10^{-5}	9.1×10^{-4}

The melting front propagation in the NePCM is positioned by employing the Stefan condition as follows:

$$u_r = \frac{k_{eff,LNeP}\frac{\partial T}{\partial r}|_{LNeP} - k_{eff,SNeP}\frac{\partial T}{\partial r}|_{SNeP}}{\varepsilon(1-\phi)\bar{\rho}_{PCM}L_{sf,PCM}} \tag{8-a}$$

$$u_z = \frac{k_{eff,LNeP}\frac{\partial T}{\partial z}|_{LNeP} - k_{eff,SNeP}\frac{\partial T}{\partial z}|_{SNeP}}{\varepsilon(1-\phi)\bar{\rho}_{PCM}L_{sf,PCM}} \tag{8-b}$$

The boundary and initial conditions for the problem are:

$$\frac{\partial T(r,0,t)}{\partial z} = \frac{\partial T(r,L,t)}{\partial z} = 0$$
$$u_r(r,0,t) = u_z(r,0,t) = 0, u_r(r,L,t) = u_z(r,L,t) = 0 \tag{9-a}$$

$$T(r_i,z,t) = T_h, u_r(r_i,z,t) = u_z(r_i,z,t) = 0 \tag{9-b}$$

$$T(r_o,z,t) = T_c, u_r(r_o,z,t) = u_z(r_o,z,t) = 0 \tag{9-c}$$

$$T(r,z,0) = T_0, u_r(r,z,0) = u_z(r,z,0) = 0 \tag{9-d}$$

As previously mentioned, the melted NePCM of the n-octadecane and $MPSiO_2$ nano-additives behaves as a power-law non-Newtonian suspension [37]. The thermophysical properties of metal foam are summarized in Table 1. The thermal conductivity of the studied NePCM in the solid and liquid phases, as well as its rheological characteristics, are given in Table 2 for the different weight concentrations of the nano-additives. Table 3 lists the thermophysical properties of n-octadecane and nano-additives. The conversion from the weight to the volume concentration was performed using the following relation:

$$\phi = \frac{\bar{\rho}_{PCM}\phi_w}{\phi_w\bar{\rho}_{PCM} + (1-\phi_w)\rho_{na}} \tag{10}$$

wherein, $\bar{\rho}_{PCM}$ denotes the average density of the pure PCM in the solid and fluid phases, and ρ_{na} is the density of the nano-additives.

Density of the NePCM:

$$\bar{\rho}_{NeP} = (1-\phi)\bar{\rho}_{PCM} + \phi\rho_{na} \tag{11}$$

Heat capacity of NePCM in the solid and fluid phases:

$$\bar{\rho}_{NeP}C_{p,LNeP} = \phi\rho_{na}C_{p,na} + (1-\phi)\bar{\rho}_{PCM}C_{p,LP} \tag{12-a}$$

$$\bar{\rho}_{NeP}C_{p,SNeP} = \phi\rho_{na}C_{p,na} + (1-\phi)\bar{\rho}_{PCM}C_{p,SP} \tag{12-b}$$

Coefficient of the thermal expansion of the NePCM in the liquid phase:

$$\bar{\rho}_{NeP}\beta_{LNeP} = \phi\rho_{na}\beta_{na} + (1-\phi)\bar{\rho}_{PCM}\beta_{LP} \tag{13}$$

The transition to the normalized space is done through the following definitions:

$$R = \frac{r}{L},\quad Z = \frac{z}{L},\quad \vec{U} = \frac{\vec{u}L}{\alpha_{LP}}, \theta = \frac{T-T_{fu}}{T_h - T_{fu}}, P = \frac{L^2 p}{\bar{\rho}_{PCM}\alpha_{LP}^2}, Fo = \frac{t\alpha_{LP}}{L^2} \tag{14}$$

The normalized equations by the use of the above definitions are as follow:

$$\nabla\cdot\vec{U} = 0 \tag{15}$$

$$\frac{1}{\varepsilon}\frac{\partial\vec{U}}{\partial Fo} + \frac{1}{\varepsilon^2}\left(\vec{U}\cdot\nabla\right)\vec{U} = \frac{\bar{\rho}_{PCM}}{\bar{\rho}_{NeP}}\nabla\cdot\left[-PI + \frac{Pr}{\varepsilon}\left[\frac{m_{LNeP}}{m_{LP}}\frac{\alpha_{Lp}^{n_{LNeP}}}{\alpha_{LP}^{n_{LP}}}\frac{L^{2n_{LP}}}{L^{2n_{LNeP}}}\right]\dot{G}^{n_{LNeP}-1}\left(\nabla\vec{U} + \left(\nabla\vec{U}\right)^{tr}\right)\right] + \vec{F} \tag{16}$$

In Eq. (16), $\dot{G}$and $\vec{F}$ are the non-dimensional shear stress tensor and vector of volume forces, respectively, defined as:

$$\dot{G} = max\left(\sqrt{[D]:[D]}, \dot{G}_{min}\right)\Big|2D = \left(\nabla\vec{U} + (\nabla\vec{U})^{tr}\right) \tag{17-a}$$

$$\vec{F} = F_R\hat{e}_R + F_Z\hat{e}_Z\begin{vmatrix} F_R = -\frac{Pr}{Da}\frac{\bar{\rho}_{PCM}}{\bar{\rho}_{NeP}}\left[\frac{m_{LNeP}}{m_{LP}}\frac{\alpha_{LP}^{n_{LNeP}}}{\alpha_{LP}^{n_f}}\frac{L^{2n_f}}{L^{2n_{LNeP}}}\right]\dot{G}^{n_{LNeP}-1}U_R \\ F_Z = -\frac{Pr}{Da}\frac{\bar{\rho}_{PCM}}{\bar{\rho}_{NeP}}\left[\frac{m_{LNeP}}{m_{LP}}\frac{\alpha_{LP}^{n_{LNeP}}}{\alpha_{LP}^{n_{LP}}}\frac{L^{2n_{LP}}}{L^{2n_{LNeP}}}\right]\dot{G}^{n_{LNeP}-1}V_R + \frac{\beta_{LNeP}}{\beta_{LP}}RaPr\theta \end{vmatrix} \tag{17-b}$$

where Darcy (Da), Prandtl (Pr), and Rayleigh (Ra) numbers are as follow:

$$Da = \frac{\kappa}{L^2}, Pr = \frac{m_{LP}}{\bar{\rho}_{PCM}}\frac{\alpha_{LP}^{n_{LP}-2}}{L^{2n_{LP}-2}}, Ra = \frac{\rho_{LP}g\beta_{LP}\Delta TL^{2n_{LP}+1}}{m_{LP}\alpha_{LP}^{n_{LP}}} \tag{18}$$

$$\left(\varepsilon\frac{\bar{\rho}_{NeP}C_{p,LNeP}}{\bar{\rho}_{PCM}C_{p,LP}} + (1-\varepsilon)\frac{(\rho C_p)_p}{\bar{\rho}_{PCM}C_{p,LP}}\right)\frac{\partial\theta}{\partial Fo} + \frac{\bar{\rho}_{NeP}C_{p,LNeP}}{\bar{\rho}_{PCM}C_{p,LP}}\left(\vec{U}\cdot\nabla\theta\right) = \left(\varepsilon\frac{k_{LNeP}}{k_{LP}} + (1-\varepsilon)\frac{k_p}{k_{LP}}\right)\nabla^2\theta \tag{19}$$

$$\left(\varepsilon\frac{\bar{\rho}_{NeP}C_{p,SNeP}}{\bar{\rho}_{PCM}C_{p,LP}} + (1-\varepsilon)\frac{(\rho C_p)_p}{\bar{\rho}_{PCM}C_{p,LP}}\right)\frac{\partial\theta}{\partial Fo} = \left(\varepsilon\frac{k_{SNeP}}{k_{LP}} + (1-\varepsilon)\frac{k_p}{k_{LP}}\right)\nabla^2\theta \tag{20}$$

Eqs. (19) and (20) are the energy equations for the liquid and solid phases of the NePCM, respectively. The melting rate of the NePCM is determined by the velocity of the progressive melting front as follows:

$$U_R = \frac{\left[\left(\varepsilon\frac{k_{LNeP}}{k_{LP}} + (1-\varepsilon)\frac{k_{SM}}{k_{LP}}\right)\frac{\partial\theta}{\partial R}|_{LNeP} - \left(\varepsilon\frac{k_{SNeP}}{k_{LP}} + (1-\varepsilon)\frac{k_{SM}}{k_{LP}}\right)\frac{\partial\theta}{\partial R}|_{SNeP}\right]Ste}{\varepsilon(1-\phi)} \tag{21-a}$$

$$U_Z = \frac{\left[\left(\varepsilon\frac{k_{LNeP}}{k_{LP}} + (1-\varepsilon)\frac{k_{SM}}{k_{LP}}\right)\frac{\partial\theta}{\partial Z}|_{LNeP} - \left(\varepsilon\frac{k_{SNeP}}{k_{LP}} + (1-\varepsilon)\frac{k_{SM}}{k_{LP}}\right)\frac{\partial\theta}{\partial Z}|_{SNeP}\right]Ste}{\varepsilon(1-\phi)} \tag{21-b}$$

for which the Stefan number (Ste) is:

$$Ste = \frac{C_{p,LP}\Delta T}{L_{sf,PCM}} \tag{22}$$

The normalized boundary and initial conditions of the problem are as follow:

$$\frac{\partial\theta(R,0,\tau)}{\partial Z} = \frac{\partial\theta(R,1,\tau)}{\partial Z} = 0 \tag{23-a}$$

$$U_R(R,0,\tau) = U_Z(R,0,\tau) = 0\ , U_R(R,1,\tau) = U_Z(R,1,\tau) = 0$$

$$\theta(R_i,Z,\tau) = 1, U_R(R_i,Z,\tau) = U_Z(R_i,Z,\tau) = 0 \tag{23-b}$$

$$\theta(R_o,Z,\tau) = \theta_c, U_R(R_o,Z,\tau) = U_Z(R_o,Z,\tau) = 0 \tag{23-c}$$

$$\theta(R,Z,0) = \theta_0, U_R(R,Z,0) = U_Z(R,Z,0) = 0 \tag{23-d}$$

Table 4
Mesh study parameters: $\varphi_w = 0.05$, $Da = 0.1$, $\varepsilon = 0.9$, $Ra = 3.93 \times 10^7$, $Ste = 0.16$, and $Pr = 51.7$.

Case No.	Elements	Melting interface elements	Computational time
1	22,120	350	13 min
2	39,809	650	20 min
3	**62,012**	**750**	**33 min**
4	83,432	1000	49 min

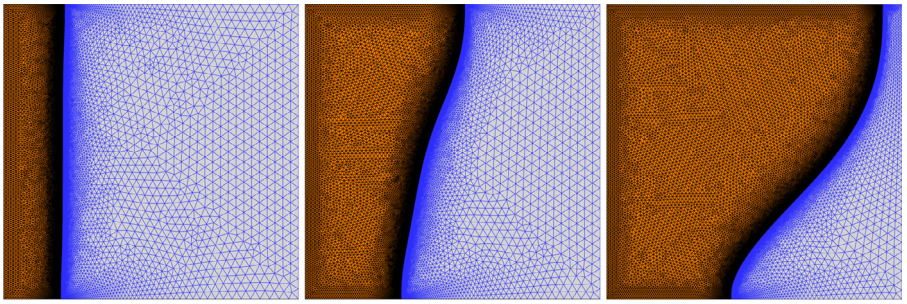

Fig. 2. Display of the used grid of Case 3 with the moving mesh technique for the melting process: (a) $Fo = 0.001$, (b) $Fo = 0.005$, and (c) $Fo = 0.015$.

The normalized fraction of the liquid NePCM is:

$$NMVF = \frac{\int_0^1 \int_{R_i}^{R_m} 2\pi R\varepsilon dRdZ}{\int_0^1 \int_{R_i}^{R_o} 2\pi R\varepsilon dRdZ} \tag{24}$$

The local Nusselt number (Nu) on the inner surface of the coaxial pipe is:

$$Nu_Z = \frac{hL}{k_{LP}} = \left(\varepsilon \frac{k_{LNeP}}{k_{LP}} + (1-\varepsilon)\frac{k_p}{k_{LP}} \right) \frac{\partial \theta}{\partial R} \Bigg)_{R=R_i} \tag{25}$$

To achieve the average Nu (Nu_{avg}) on the hot wall, Eq. (25) is integrated along the z-direction:

$$Nu_{avg} = \int_o^1 Nu_z dz \tag{26}$$

The time-averaged Nu_{avg} is evaluated as:

$$\overline{Nu_{avg}} = \frac{\int_o^{Fo_{\max}} Nu_{avg} dFo}{Fo_{max}} \tag{27}$$

in which Fo_{max} is the time of the melting process and $NMVF_{max}$ is the melted fraction volume at the end of the melting process.

3. Numerical approach and grid test

The equations to model the melting of a NePCM with the non-Newtonian power-law melted liquid, i.e. Eqs. (15)–(17) and Eqs. (18)–(21), are fully non-linear and coupled. Hence, in this research, we employed the robust procedure of the Galerkin finite element method to solve them. This method can be found in detail in [44]. An unstructured mesh made up of triangular elements was utilized because these elements are better adapted to the curved phase-change interface. To test the independence of the mesh, four different grid sizes were examined (Table 4). The deformed mesh technique with re-meshing over time was used to track the solid–liquid phase fronts (Fig. 2). The variations in velocity of the melting front, normalized melt volume fraction ($NMVF$), and Nu_{avg} were very slight (Fig. 3), while the grid of case 3 was further refined to case 4. There was no distinct discrepancy between the grids of cases 3 and 4, but the latter was more computationally demanding. Consequently, the grid size of case 3 was adopted in the calculations.

To examine the verification and validation of the utilized numerical procedure and the correctness of our modeling, the simulated outcomes of this work were compared to the other numerical and experimental studies in the literature [45–49]. The verification and validation tried to cover all the aspects of the problem.

A comparison was performed for the melting of coconut oil–CuO NePCMs embedded in an aluminum metal foam [49]. The long-term stability of the coconut oil–CuO was tested for more than six months, and it was found that the NePCM could be stable. Excellent cycling stability was also reported with a very small amount of sedimentation. The thermophysical

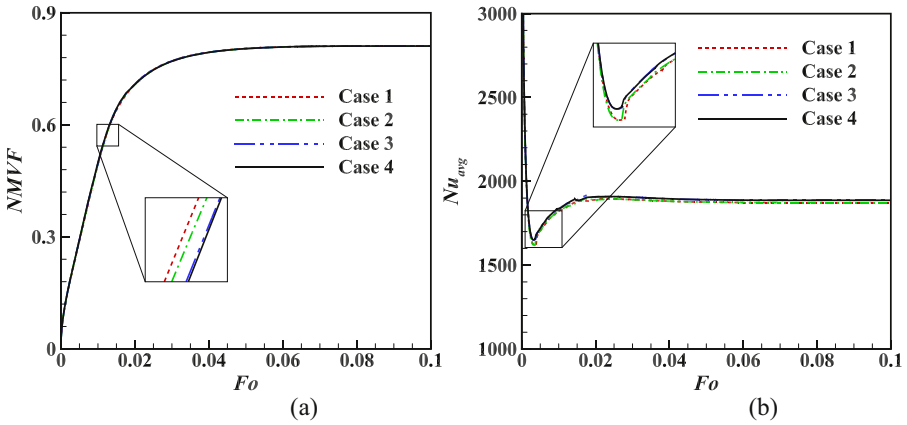

Fig. 3. (a) Normalized melted volume fraction (*NMVF*) of the liquid NePCM and (b) average Nusselt number (Nu_{avg}) variations over time (φ_{wt}= 0.05, Da = 0.1, ε= 0.9) for Cases 1–4.

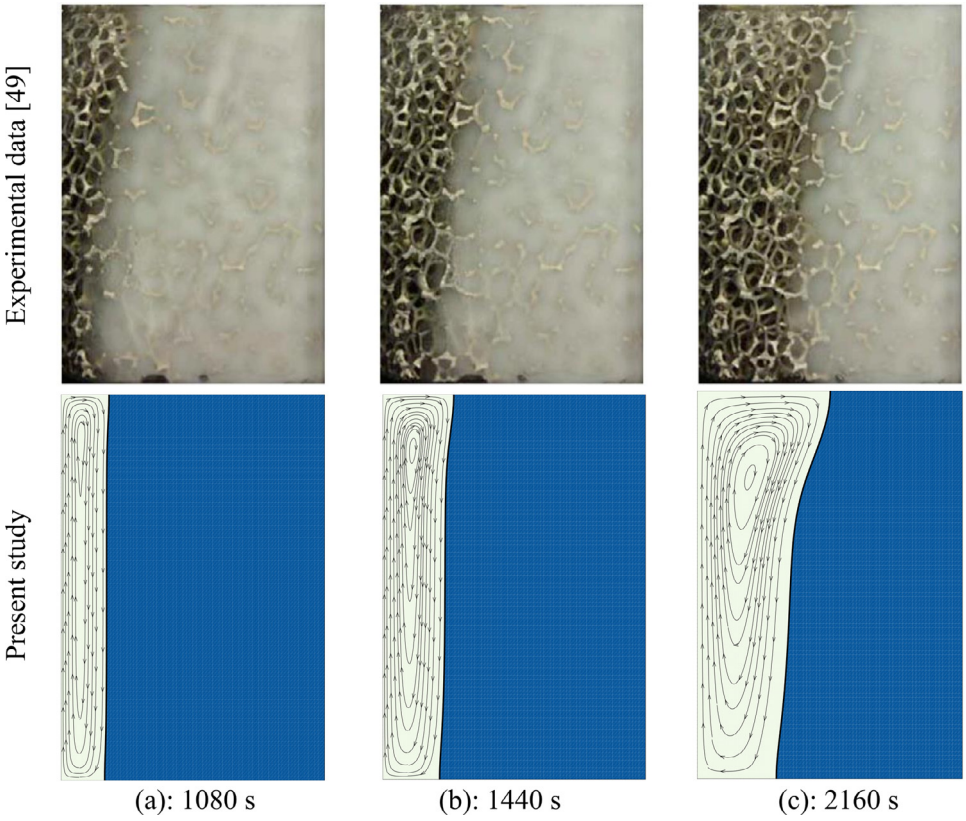

Fig. 4. Comparison of the melting interface between previous experimental results [49] and the numerical results of the present study for coconut oil embedded in an aluminum metal foam.

properties of coconut oil–CuO and the metal foam are reported in Table 3 of [49]. The geometry of the test module was an enclosure of 7.2 cm (height) × 5.0 cm (width). All walls were insulated except the left wall, which was subject to a constant heat flux. The initial temperature of the PCM and porous matrix was 20°C. Following the inspection of melting fractions in the visual images and considering the change of element's electrical resistance, the net value of the imposed heat flux at the hot surface was found as $q'' = 1075$ W/m^2. The porosity was $\varepsilon = 0.92$, and the permeability was computed as $K = 3.3142 \times 10^{-7}$ m^2 for the given pore density of 5 PPI [50–52]. A comparison between the experimental results of Fig. 3(a) in [49] and the present numerical simulations shows that the numerical simulations and experimental observations were in very good agreement (Fig. 4).

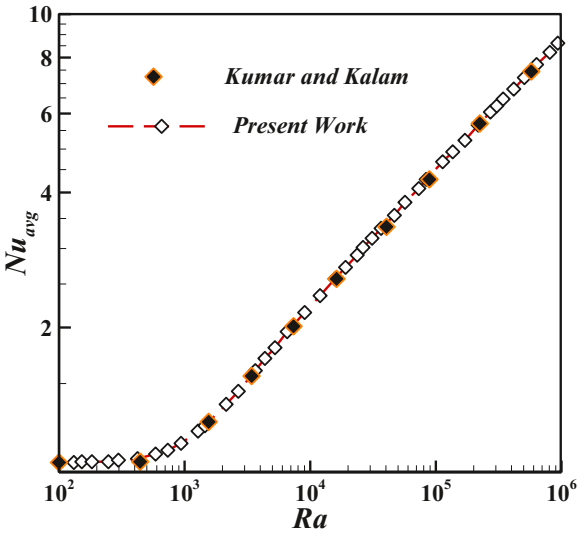

Fig. 5. Dependency of the average Nusselt number (Nu_{avg}) on Ra for the present work and from Kumar and Kalam [45].

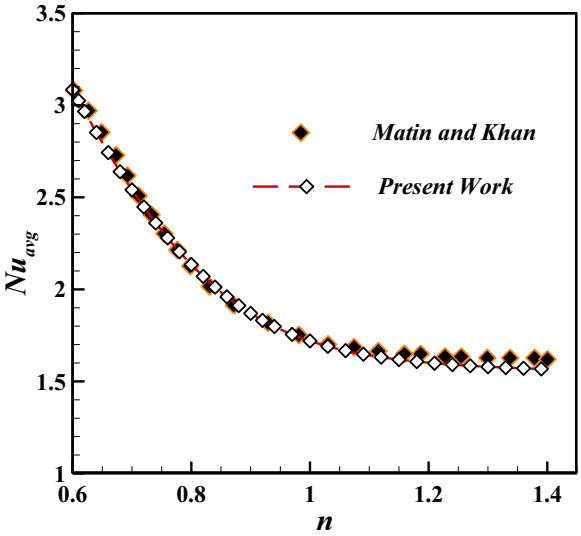

Fig. 6. Dependency of average Nusselt number (Nu_{avg}) on the power-law index, i.e. n, of this study and Matin and Khan [46] when $Ra = 10^3$ and $Pr = 10$.

The verification of the modeling of the free convection inside a coaxial pipe was examined by comparing our results with those of Kumar and Kalam [45], which showed that the dimensions and boundary conditions were the same for both (Fig. 5). In fact, in the studied coaxial pipe, the high and low temperature of T_h and T_c were imposed on the inner and outer walls. However, the upper and lower walls were well adiabatic. The ratio of the outer radius to the inner radius of the pipe was 1. Additionally, the aspect ratio, i.e. the ratio of the difference between the outer and inner radius to the height of pipe was 1. The working fluid flowing in the enclosed medium was air with Pr of 0.71. The buoyancy-driven flow of a power-law liquid within an enclosed medium was verified using the numerical work of Matin and Khan [46]. The enclosed medium contained a horizontal cylindrical annulus having the hot inner and cold outer bounds. The ratio of the outer radius to the inner radius was 2.5. The working liquid had $Pa = 10$ and $Ra = 10^3$, respectively; it is worth noting that the characteristic length for Pa and Ra was the difference between the outer and inner radii. The Nu_{avg} for the present and a previous study [46] for different values of the power-law indexes are presented in Fig. 6.

Validation and verification of the deformed mesh model employing the Stefan condition to simulate the phase-change process were conducted with the experimental and numerical results acquired by several studies in [47]. The computational domain was a rectangular cuboid enclosure of 88.9 mm high, 63.5 mm wide, and 38.1 mm deep. The left and right side walls of the medium were fully active with hot and cold temperatures, while the other walls were adiabatic. The PCM used in the experimental study was gallium with a purity of 99.6%, and a melting point of 302.93 K. The comparison shown in Fig. 7

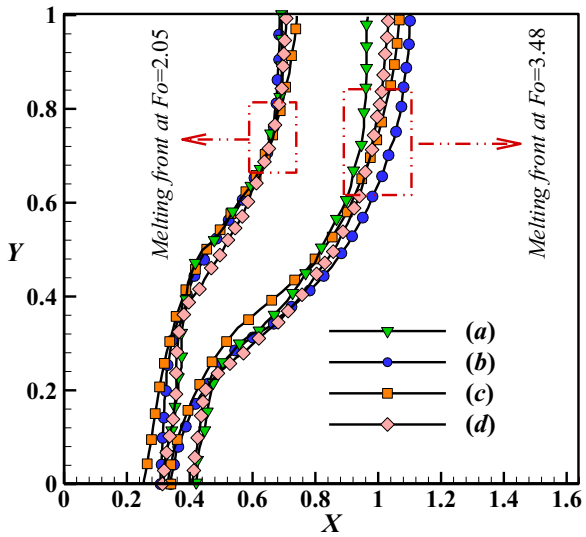

Fig. 7. The progressive melting front acquired by studies reported in [47]: (a) Kashani et al., (b) Gau and Viskanta, and (c) Brent et al.; and (d) the present study for $Ra = 6 \times 10^5$, $Ste = 0.039$, and $Pr = 0.0216$.

Table 5
Average Nusselt number of the present investigation and that of [48].

Ra	Da	ε	Reference [48]	Present study
10^7	10^{-4}	0.9	9.202	9.322
10^5	10^{-2}	0.9	3.910	3.920

was conducted for $Ra = 6 \times 10^5$, $Ste = 0.039$, and $Pr = 0.0216$. Finally, to ensure the correctness of the natural convection modeling in a porous medium considering the local thermal equilibrium condition, our numerical code was further verified with the data reported in [48]. The computational domain in this comparison was a square enclosure, in which the left and right walls were subjected to hot and cold temperatures, respectively. However, the other walls were adiabatic. The Darcy–Brinkman–Forchheimer equations were used to model the Newtonian-fluid flow in the porous medium. The Pr of the fluid-saturated in the pores was 1. According to the evaluations presented in Figs. 4–7 and Table 5, the developed code was reliable to continue the calculations.

4. Results and discussion

The free convection melting of a non-Newtonian PCM enhanced with $MPSiO_2$ nanoparticles inside a porous enclosure was numerically explored. The size of the cavity was considered to be $L = 45$ mm. The hot and cold surfaces were considered to be kept isothermally at $T_h = 45°C$ and $T_c = 25°C$. The melting temperature is reported to be 27.5°C [31]. Accordingly, the non-dimensional parameters for the base PCM were evaluated as $Ra = 3.9 \times 10^7$, $Pr = 51.7$, and $Ste = 0.158$.

In the present study, the impact of dispersion of $MPSiO_2$ nanoparticles in the PCM ($0.0 \leq \varphi_{wt} \leq 0.05$), the porosity of the solid matrix ($0.3 \leq \varepsilon \leq 0.9$), and Da ($10^{-4} \leq Da \leq 10^{-1}$) on the patterns of the streamlines and isotherms, melting rate, and Nu_{avg} were investigated.

The influence of the nanoparticles' mass fraction on the patterns of isotherms and streamlines of the melted PCM for different Fourier numbers is depicted in Fig. 8. The phase-change process proceeds as time elapses and the melted area develops. It is noteworthy that as the fusion temperature was higher than the cold wall temperature, the entire domain would not melt. In fact, the heat would be transferred to the cold wall through the solid phase and by the conduction mechanism when the steady-state condition was achieved. The isothermal lines were vertical at the early stages of melting as the conduction mode was dominant in the cavity. As time elapsed, the melt volume fraction increased and the flow rate increased, resulting in a distortion in the fluid isotherms, indicating an augmentation in the convection share of heat transfer. According to experimental data [31] (Table 2), adding the nanoparticles to the PCM affects the flow and thermal fields as it alters the rheological and thermophysical characteristics of the NePCM. It was evident that dispersion of $MPSiO_2$ nanoparticles slightly increased the thermal conductivity of the solid and liquid phases and decreased the power-law index of the NePCM. However, the consistency index of the NePCM increased considerably, meaning that apparent viscosity of the NePCM was significantly augmented. Hence, the convection heat transfer was retarded, resulting in the lower melting rate of the NePCM. As a result, the fluid strength and, consequently, the distortion of the isothermal lines declined by increasing the mass fraction of the nanoparticles.

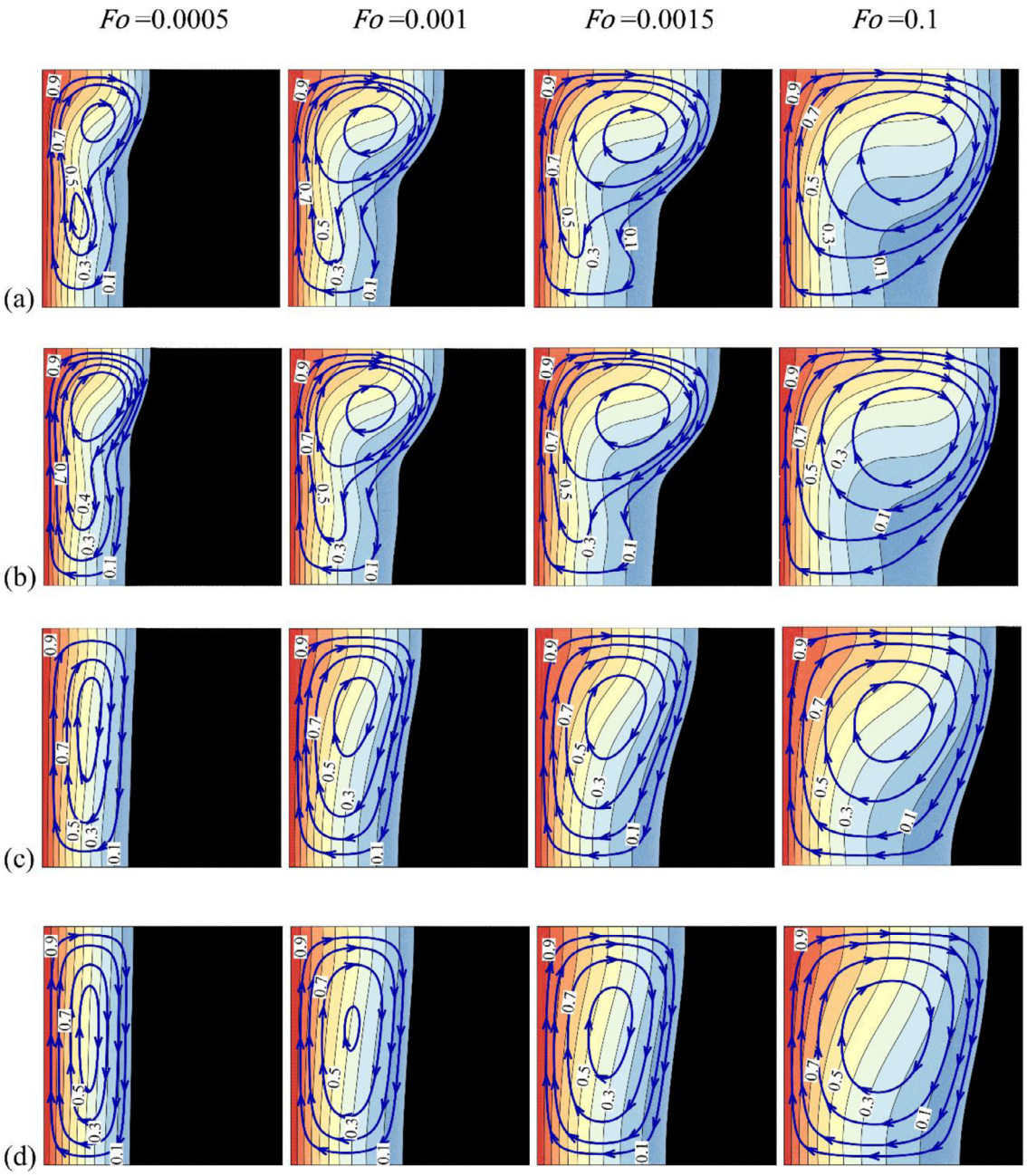

Fig. 8. Impact of the nanoparticles' mass fraction on the streamlines and isotherms of the melting NePCM when $\varepsilon = 0.5$ and $Da = 0.01$ for nanoparticle mass fraction of (a) 0.00, (b) 0.01, (c) 0.03, and (d) 0.05.

To analyze the influence of the $MPSiO_2$ particles in the PCM more precisely, the melting fronts of Fig. 8 are illustrated in Fig. 9. Evidently, at each non-dimensional time, the maximum melted fraction ($NMVF_{max}$) was for the case of $\varphi_{wt} = 0.00$, with its minimum when $\varphi_{wt} = 0.05$. In fact, adding the nano-sized particles to the PCM increased the apparent viscosity and the thermal conductivity of the NePCM, in which the former lowered the convection share of heat transfer and the latter boosted the conduction mechanism. As the distortion of the melting fronts decreased with augmentation of the nanoparticle mass fraction, it can be concluded that increasing φ_{wt} reduced the heat transfer rate. Additionally, the melting front for the cases of $\varphi_{wt} = 0.00$ and 0.01 approximately coincided, as the 1% concentration of $MPSiO_2$ only slightly increased the consistency index of the fluid phase, and the resulting melted NePCM still behaved as a Newtonian fluid.

Time variation of *NMVF* of the melted PCM and Nu_{avg} for different values of nanoparticle concentration is outlined in Fig. 10(a) and (b), respectively. The melting process clearly ceased and reached its steady-state condition at $Fo \approx 0.01$ for

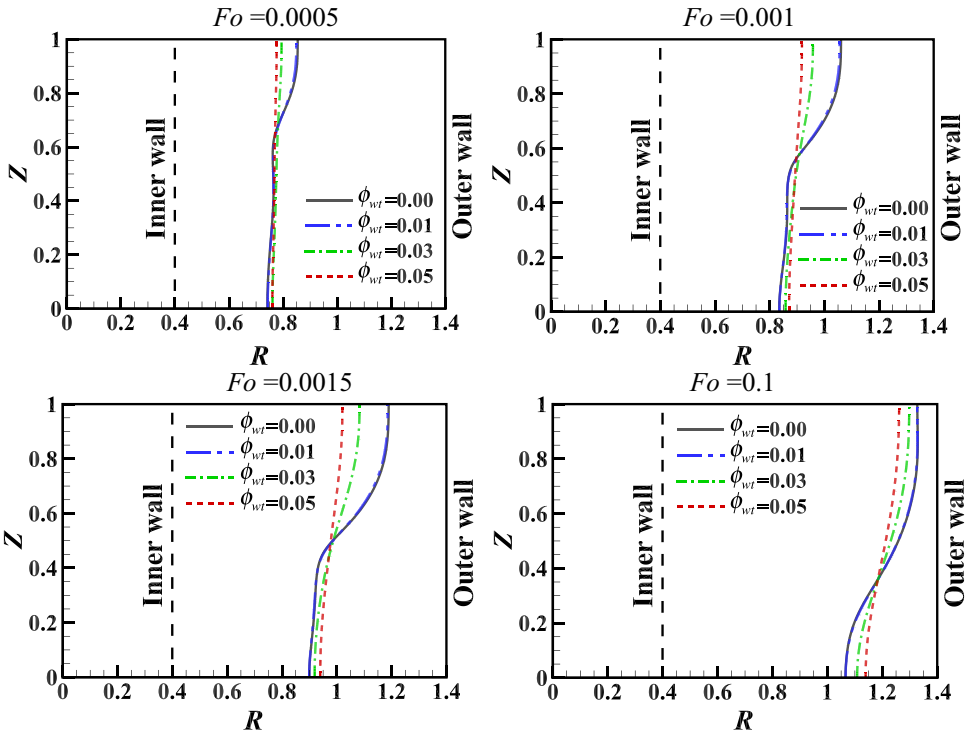

Fig. 9. Dependency of the melting front on the non-dimensional mass fraction of the nanoparticles for different dimensionless times when $\varepsilon = 0.5$ and $Da = 0.01$.

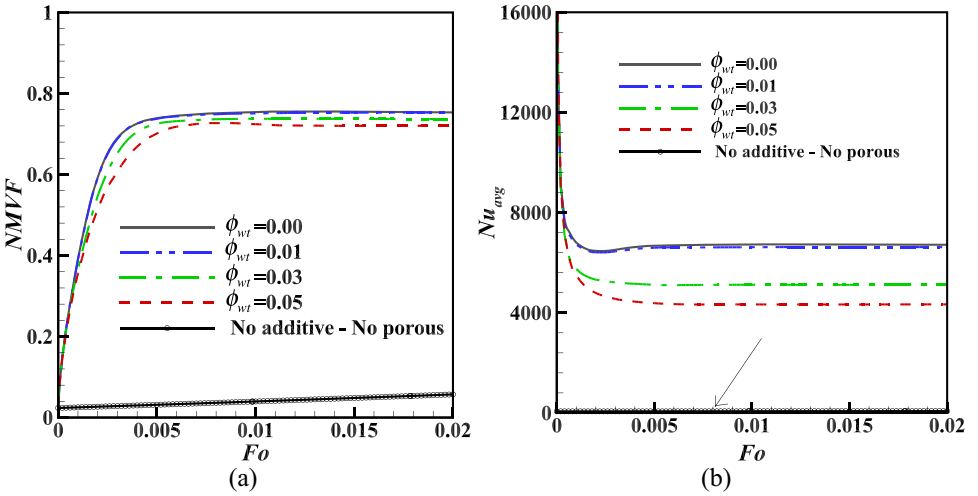

Fig. 10. The impact of the nanoparticle mass fraction for the case of $\varepsilon = 0.5$ and $Da = 0.01$ on (a) normalized melted volume fraction (*NMVF*) and (b) average Nusselt number (Nu_{avg}).

all nanoparticle concentrations (Fig. 10(a)). Moreover, increasing the concentration of $MPSiO_2$ decreased *NMVF*. An increase in the mass fraction of the nano-sized particles lowered the heat transfer rate (Fig. 10(b)). Based on what was discussed previously concerning the increment of apparent viscosity of the NePCM with increasing φ_{wt}, it is clear that the heat transfer rate decreased, because the convection share of the overall heat transfer was reduced.

Since there was a charging flow of thermal energy through the hot wall and energy disgorge flowed from the cold wall, the net amount of stored thermal energy can be considered as latent heat. The heat graphs depict *NMVF* of melted PCM in the enclosure (Fig. 10). Thus, the normal stored thermal energy in the enclosure can be estimated by $(1 - \varphi_{wt}) \times NMVF$. The term $(1 - \varphi_{wt})$ was multiplied by *NMVF* since the nanoparticles did not contribute to latent thermal energy storage.

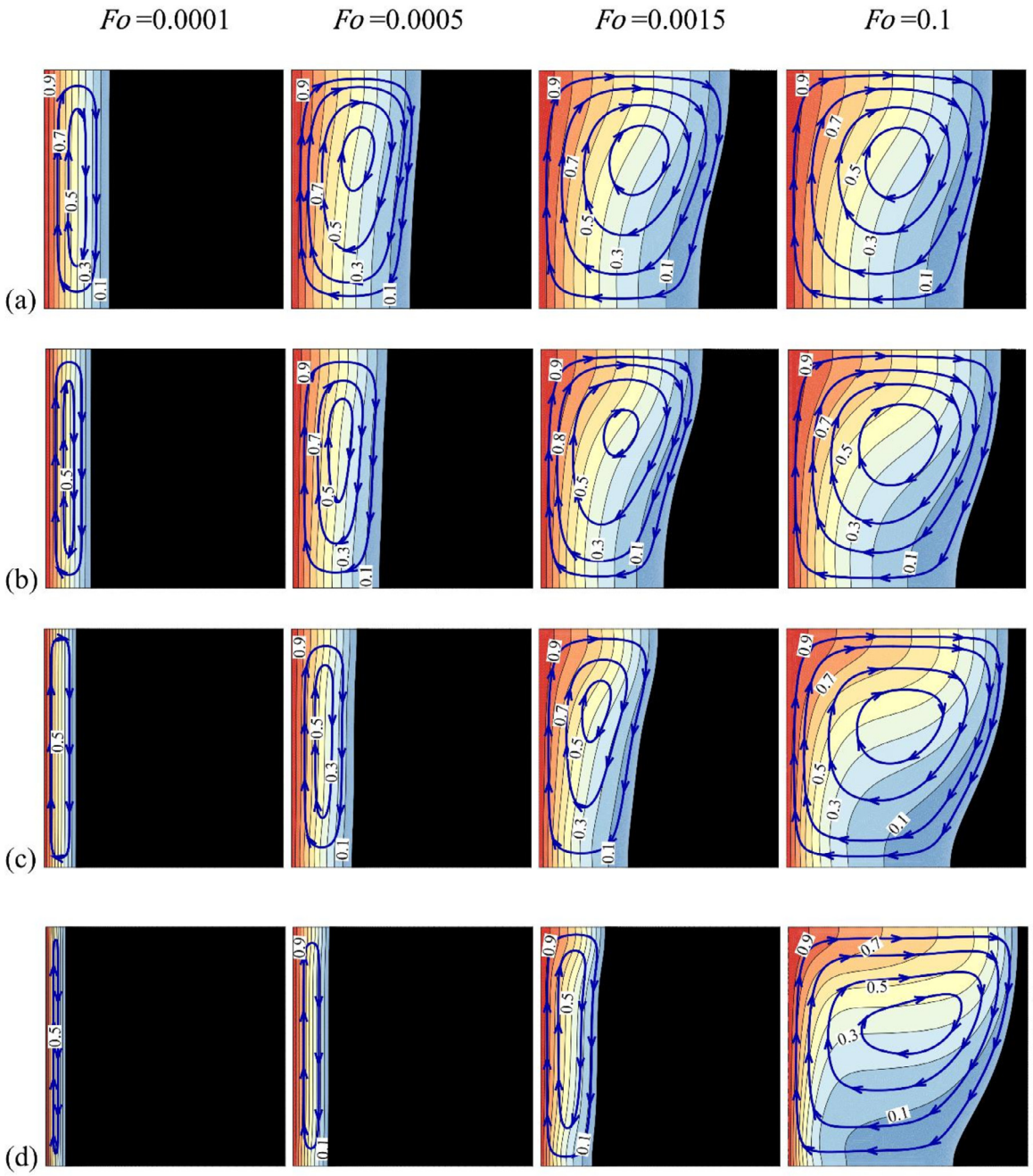

Fig. 11. The impact of the porosity on the streamlines and isotherms of the melting NePCM when $\varphi_{wt} = 0.03$ and $Da = 0.01$ for porosity values of (a) $\varepsilon = 0.3$, (b) $\varepsilon = 0.5$, (c) $\varepsilon = 0.7$, and (d) $\varepsilon = 0.9$.

Fig. 11 illustrates the effect of the porosity of the solid matrix on the patterns of the streamlines and the isothermal lines of the melted NePCM, in four separate Fourier numbers. The isotherms and melting front were uniformly vertical at low values of non-dimensional time, indicating that the conduction mechanism completely controlled the phase change. As time elapsed, the isothermal lines distorted, which characterized the intensification of the convection heat transfer. The melting fronts of the presented contours of Fig. 11 are plotted in Fig. 12 for further analysis.

The porosity of a solid matrix affected the melting front in different ways because the melted area of the case $\varepsilon = 0.9$, which was the least Fourier number, overtook the other case of high Fourier number ($Fo = 0.1$ or the steady-state case) (Fig. 12). This can be explained by the fact that the porosity of the solid matrix acted as a resistance against the molten liquid flow and reduced its momentum, thus increasing the porosity and enhancing the convection mode of heat transfer.

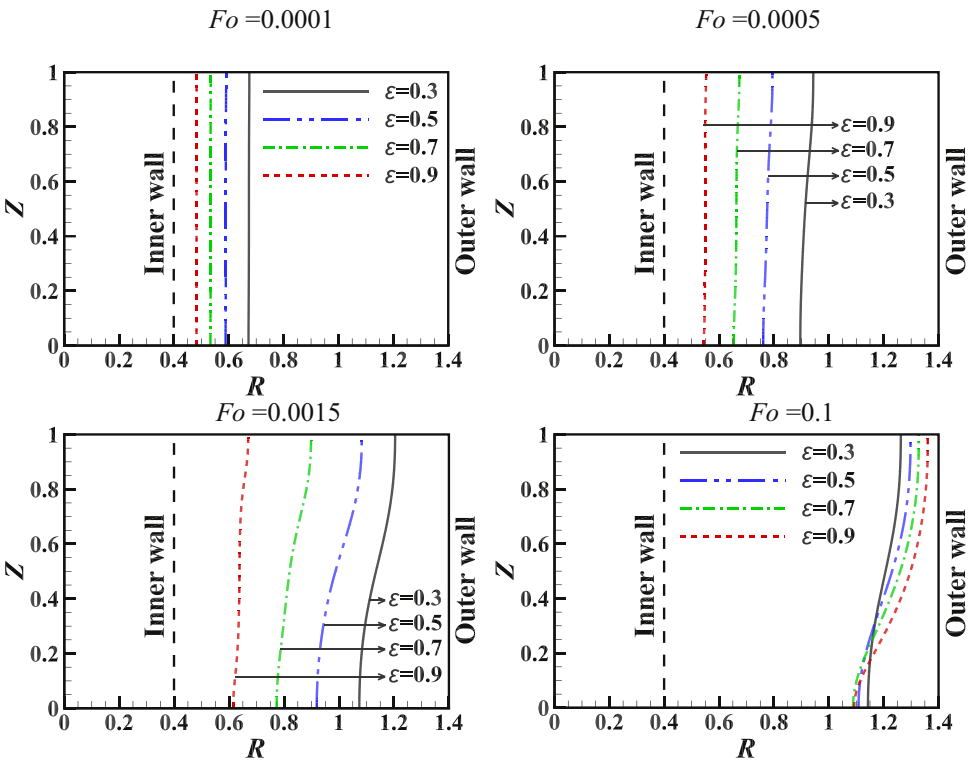

Fig. 12. The dependency of the melting front on the porosity of the solid matrix at certain non-dimensional times when φ_{wt} = 0.03 and Da = 0.01.

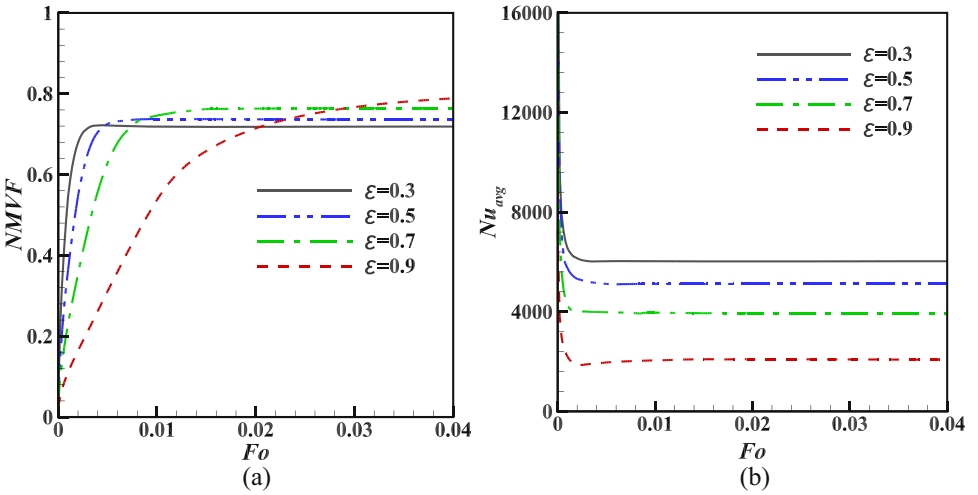

Fig. 13. The impact of porosity of the solid matrix for the case of φ_{wt} = 0.03 and Da = 0.01 on (a) normalized melted volume fraction (*NMVF*) and (b) average Nusselt number (Nu_{avg}).

On the other hand, generally, raising the porosity retards the effective thermal conductivity of the medium since the thermal conductivity of the solid matrix is much greater than of the fluid. Therefore, increasing porosity reduced the conduction mechanism and thus lowered the heat transfer. At the early stages of melting, i.e. low Fourier numbers, a lower amount of NePCM melted when the porosity of the porous matrix was higher. This was associated with the lower effective thermal conductivity of the NePCM and the dominance of the conduction mode of heat transfer at the early stages of the phase change process. However, as the melting process continued, the fluid flow and convection share of heat transfer were augmented. For high values of porosity, the impact of porosity on the fluid flow was a minimum. Thus when the convection mode prevailed over conduction, the melted fraction intensified strongly.

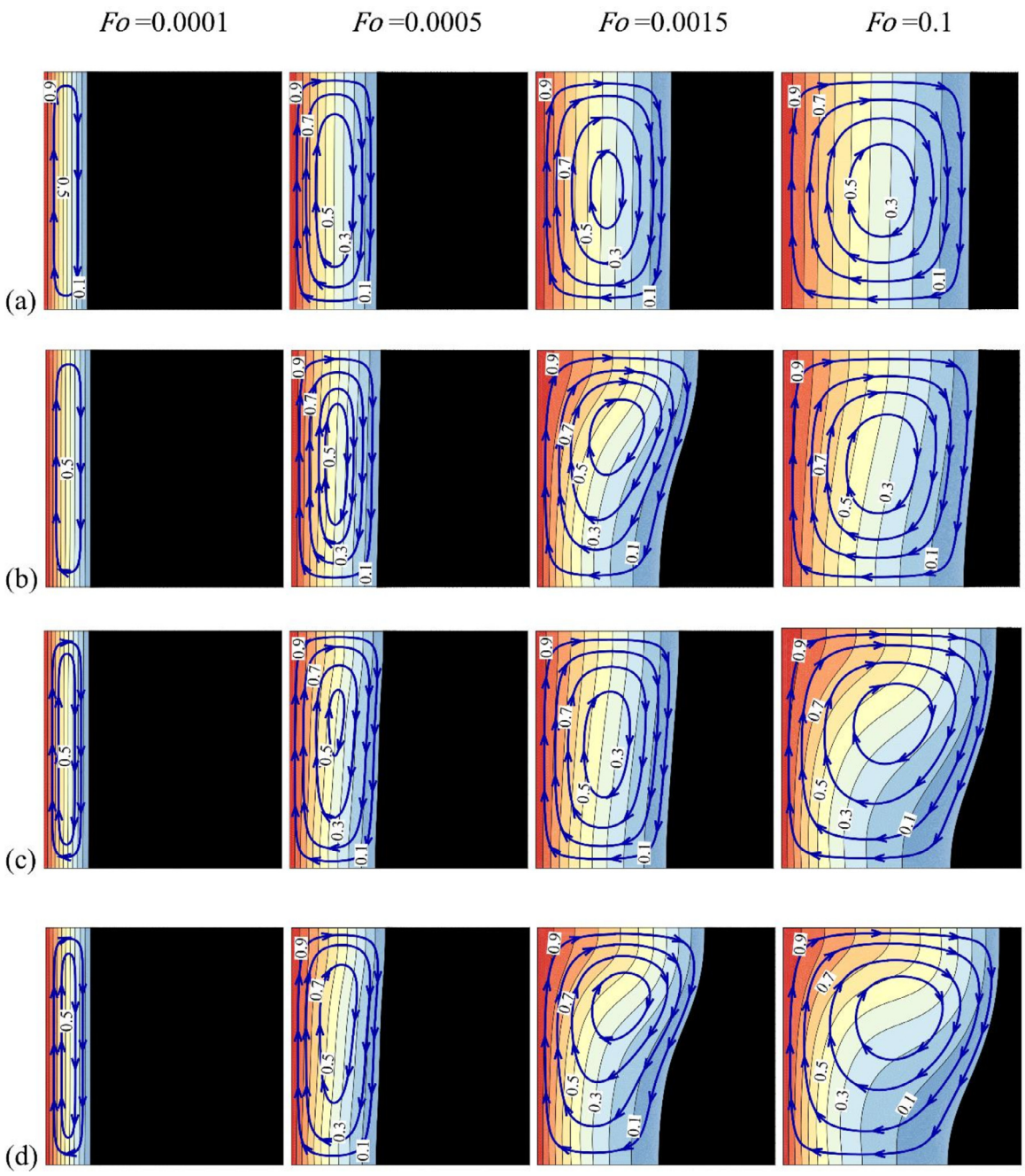

Fig. 14. The dependency of the streamlines and isotherms of the melting PCM on the Darcy number (Da) when $\varphi_{wt} = 0.03$ and $\varepsilon = 0.5$ and Da values of (a) 0.0001, (b) 0.001, (c) 0.01, and (d) 0.1.

The *NMVF* and Nu_{avg} varied with non-dimensional time and showed that the melting rate robustly depended on porosity of the porous medium (Fig. 13). As discussed earlier, the melted fraction of the NePCM was amplified as porosity increased. This intensification was so strong that the *NMVF* for the case of $\varepsilon = 0.9$, which was much lower than the others when $Fo \leq 0.02$, overtook the other items as the Fourier number rose (Fig. 13(a)). In addition, an increment of the porosity raised the required time to reach the steady-state condition. This is because by increasing porosity, the convection heat transfer increased, and so a higher amount of NePCM was melted. Hence, the melting process took longer to approach the steady-state condition. Despite augmentation of the fluid flow and melting rate of the NePCM, the heat transfer rate declined with increasing porosity. This can be explained by considering the fact that the effective thermal conductivity of the NePCM, according to Eq. 27, decreased as ε increased.

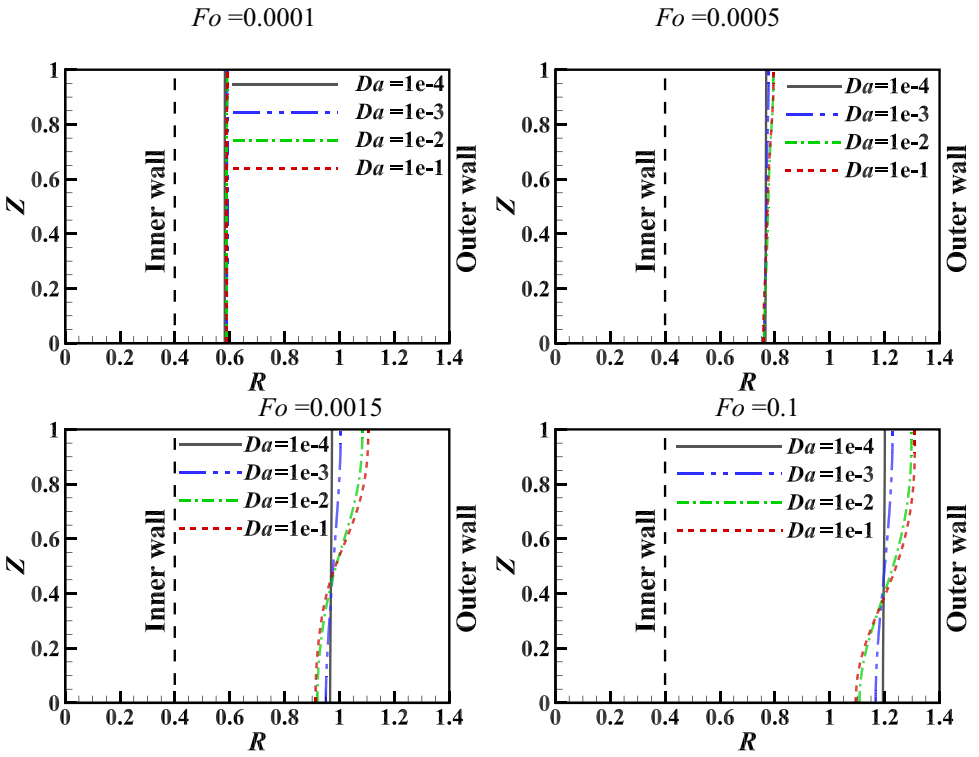

Fig. 15. The dependency of the melting front on the Darcy number (Da) for non-dimensional times when $\varphi_{wt} = 0.03$ and $\varepsilon = 0.5$.

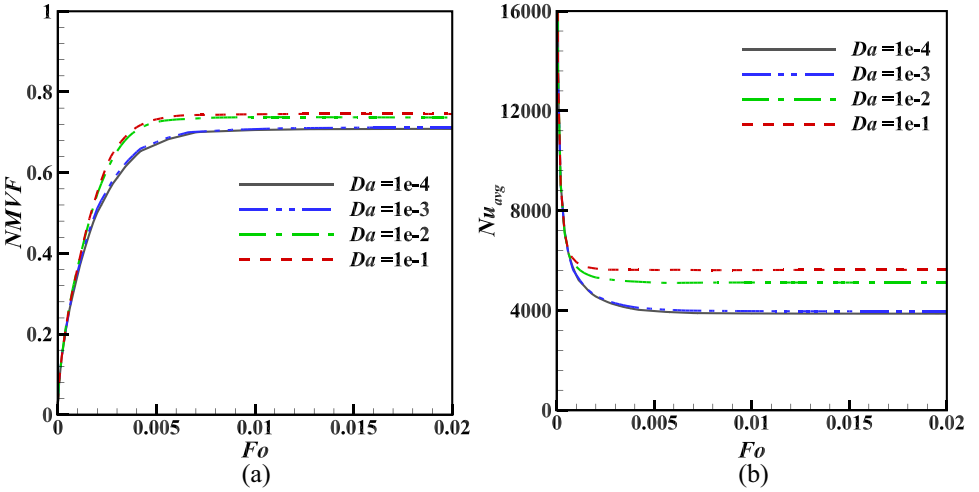

Fig. 16. The impact of Darcy number (Da) when $\varphi_{wt} = 0.03$ and $\varepsilon = 0.5$ on (a) normalized melted volume fraction ($NMVF$) and (b) average Nusselt number (Nu_{avg}).

Fig. 14 depicts the influence of Da on the patterns of the streamlines and isotherms for different non-dimensional times, and Fig. 15 outlines their corresponding melting fronts. The Da characterizes permeability of the porous matrix, and therefore the fluid flow rose as it increased. For low values of Da, the isotherms remained completely vertical throughout the phase-change process (follow the solid blue lines of $Da = 10^{-4}$ in Fig. 15), specifying that the conduction governed the way that heat was transferred. However, by increasing Da, the ability of the porous matrix to transmit the melted NePCM increased, and thus, for higher Da values, the melted region enlarged, and the isotherms distorted, specifying an augmentation in the convection heat transfer. In addition to this, all melting fronts almost coincided when $Fo \leq 0.0005$, indicating the conduction stage of the melting process.

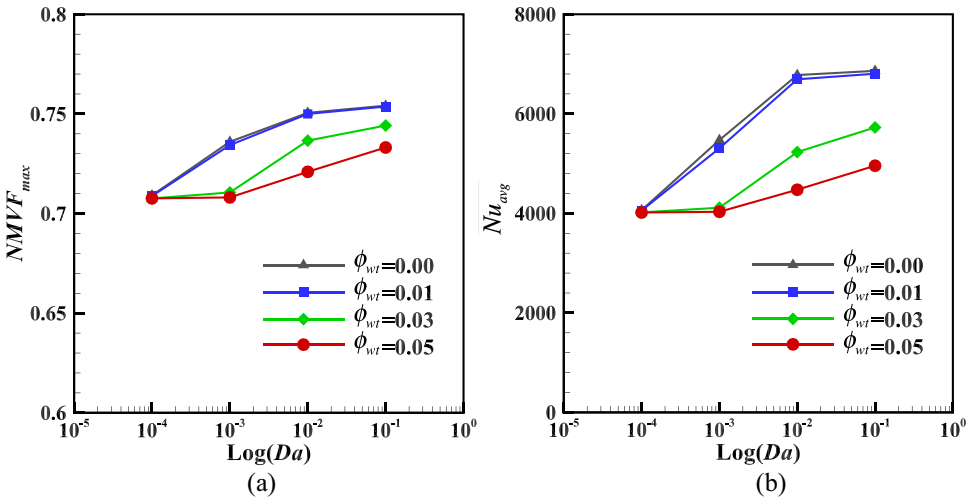

Fig. 17. The impact of Darcy number (*Da*) and nanoparticle mass fraction at the end of the melting process when $\varepsilon = 0.5$ on (a) *NMVF* and (b) time-averaged *Nu*.

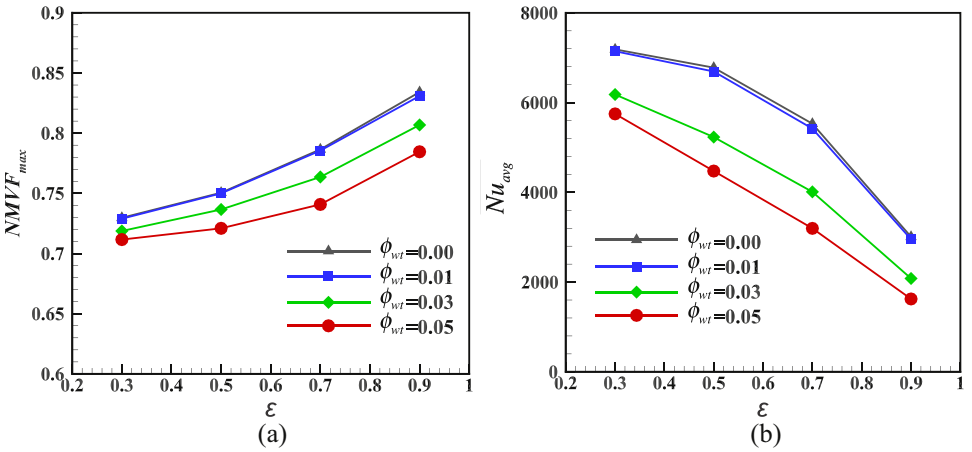

Fig. 18. The impact of porosity and nanoparticle mass fraction at the end of the melting process when $Da = 0.01$ on (a) *NMVF* and (b) time-averaged *Nu*.

Time variation of *NMVF* of the studied PCM and its Nu_{avg} for different values of *Da* showed a direct correlation between *NMVF* and permeability of the porous medium (Fig. 16). This is reasonable because augmentation of *Da* boosted the fluid flow and thus intensified the rate of natural convection heat transfer. Consequently, Nu_{avg} increased with the increment of *Da*.

The $NMVF_{max}$ at the end of the melting process and the time-averaged *Nu* for different values of the studied parameters are presented in Figs 17 and 18. The volume fraction of the melted NePCM at the steady-state condition increased with the increment of *Da* as it intensified the fluid flow and convection heat transfer in the cavity (Fig. 17). Moreover, increasing the mass fraction of the nanoparticles reduced $NMVF_{max}$ as it increased the apparent viscosity of the liquid PCM. The time-averaged *Nu* also increased with rising *Da* and declined with the increment of the nanoparticle mass fraction. An increase in porosity of the porous medium increased $NMVF_{max}$ of the melted PCM as it reduced the resistance of the porous matrix to fluid flow (Fig. 18). Nonetheless, the time-averaged *Nu* declined with increasing porosity as it reduced the effective thermal conductivity of the medium.

5. Conclusion

The phase transition process of a non-Newtonian NePCM between two concentric cylinders was analyzed numerically. The host PCM was considered to be n-octadecane and enhanced with $MPSiO_2$ nanoparticles. The porous medium was considered to be homogeneous and made from aluminum foam. According to the literature, the melted NePCM exhibited shear-thinning behavior and thus was modeled as a power-law fluid. The non-linear coupled equations governing the flow and thermal fields were first non-dimensionalized and then solved using the Galerkin finite element method. Moreover, to cap-

ture the melting front, the deformed mesh technique was employed. The influence of the volume fraction of the nanoparticles, *Da*, and porosity of the solid matrix was surveyed, and the following conclusions drawn:

1. Adding $MPSiO_2$ nanoparticles lowered the fluid strength and the distortion of the isothermal lines as it altered the rheological and thermophysical characteristics of the NePCM.
2. Increasing the mass fraction of $MPSiO_2$ nanoparticles reduced the rate of heat transfer as it diminished the fluid flow and convection mode of heat transfer.
3. Increasing porosity of the porous matrix lowered Nu_{avg}. Additionally, increasing *Da* raised *NMVF* and also intensified the heat transfer rate.
4. The $NMVF_{max}$ of the NePCM increased with the increment of *Da* and the porosity of the medium, and decreased as the mass fraction of nanoparticles rose.
5. The time-averaged *Nu* showed an upward trend with augmentation of *Da* and dropped as porosity of the solid matrix and the mass fraction of the $MPSiO_2$ nanoparticles increased.

CRediT author statement

S.A.M. Mehryan: Conceptualization, Methodology, Supervision, Investigation, **M. Ghalambaz:** Conceptualization, Methodology, Supervision, Validation, Writing – Review & Editing, **M. Vaezi:** Writing Original draft preparation. **S. M. Hashem Zadeh:** Conceptualization, Methodology, Investigation, Writing – Review & Editing. **N. Sedaghatizadeh:** Writing Original draft preparation, Investigation. **O. Younis,** Conceptualization, Writing – Review & Editing. **A. J. Chamkha:** Methodology, Writing – Review & Editing. Validation, Investigation. **H. Abulkhair:** Methodology, Writing – Review & Editing, Investigation.

References

[1] K.J. Chua, S.K. Chou, W.M. Yang, J. Yan, Achieving better energy-efficient air conditioning – A review of technologies and strategies, Appl. Energy 104 (2013) 87–104.
[2] I. Sarbu, C. Sebarchievici, A comprehensive review of thermal energy storage, Sustainability 10 (2018) 191.
[3] A. Joseph, M. Kabbara, D. Groulx, P. Allred, M.A. White, Characterization and real-time testing of phase-change materials for solar thermal energy storage, Int. J. Energy Res. 40 (2015) 61–70.
[4] K. Swaminathan Gopalan, V. Eswaran, Numerical investigation of thermal performance of PCM based heat sink using structured porous media as thermal conductivity enhancers, Int. J. Thermal Sci. 104 (2016) 266–280.
[5] S.M. Shalaby, M.A. Bek, A.A. El-Sebaii, Solar dryers with PCM as energy storage medium: A review, Renew. Sust. Energ. Rev. 33 (2014) 110–116.
[6] M.J. Hosseini, M. Rahimi, R. Bahrampoury, Experimental and computational evolution of a shell and tube heat exchanger as a PCM thermal storage system, Int. Commun. Heat Mass Transf. 50 (2014) 128–136.
[7] J. Yu, Y. Yang, X. Yang, Q. Kong, L. Yanhua, J. Yan, Effect of porous media on the heat transfer enhancement for a thermal energy storage unit, Energy Procedia 152 (2018) 984–989.
[8] A. Mills, M. Farid, J.R. Selman, S. Al-Hallaj, Thermal conductivity enhancement of phase change materials using a graphite matrix, Appl. Therm. Eng. 26 (2006) 1652–1661.
[9] M.A. Kibria, M.R. Anisur, M.H. Mahfuz, R. Saidur, I.H.S.C. Metselaar, A review on thermophysical properties of nanoparticle dispersed phase change materials, Energy Convers. Manag. 95 (2015) 69–89.
[10] S. Mousavi, M. Siavashi, M.M. Heyhat, Numerical melting performance analysis of a cylindrical thermal energy storage unit using nano-enhanced PCM and multiple horizontal fins, Numer. Heat Tr. A-Appl. 75 (2019) 560–577.
[11] H. Xu, Z. Xing, K. Vafai, Analytical considerations of flow/thermal coupling of nanofluids in foam metals with local thermal non-equilibrium (LTNE) phenomena and inhomogeneous nanoparticle distribution, Int. J. Heat Fluid Flow 77 (2019) 242–255.
[12] H.J. Xu, Z.B. Xing, F. Wang, Z. Cheng, Review on heat conduction, heat convection, thermal radiation and phase change heat transfer of nanofluids in porous media: Fundamentals and applications, Chem. Eng. Sci. 195 (2019) 462–483.
[13] S. Mancin, A. Diani, L. Doretti, K. Hooman, L. Rossetto, Experimental analysis of phase change phenomenon of paraffin waxes embedded in copper foams, Int. J. Therm. Sci. 90 (2015) 79–89.
[14] X. Xiao, P. Zhang, M. Li, Preparation and thermal characterization of paraffin/metal foam composite phase change material, Appl. Energy 112 (2013) 1357–1366.
[15] M.M. Heyhat, S. Mousavi, M. Siavashi, Battery thermal management with thermal energy storage composites of PCM, metal foam, fin and nanoparticle, J. Energy Storage 28 (2020) 101235.
[16] A.H. Sweidan, Y. Heider, B. Markert, Modeling of PCM-based enhanced latent heat storage systems using a phase-field-porous media approach, Contin. Mech. Thermodyn. 32 (2019) 861–882.
[17] H. Xu, Y. Wang, X. Han, Analytical considerations of thermal storage and interface evolution of a PCM with/without porous media, Int. J. Numer. Method H. 30 (2019) 373–400.
[18] S.K. Das, S.U. Choi, W. Yu, T. Pradeep, Nanofluids: Science and Technology (2007).
[19] J.M. Khodadadi, L. Fan, H. Babaei, Thermal conductivity enhancement of nanostructure-based colloidal suspensions utilized as phase change materials for thermal energy storage: A review, Renew. Sust. Energ. Rev. 24 (2013) 418–444.
[20] H. Yang, S.A. Memon, X. Bao, H. Cui, D. Li, Design and preparation of carbon based composite phase change material for energy piles, Materials 10 (2017) 391.
[21] N.S. Bondareva, N.S. Gibanov, M.A. Sheremet, Computational study of heat transfer inside different PCMs enhanced by Al_2O_3 nanoparticles in a copper heat sink at high heat loads, Nanomaterials 10 (2020) 284.
[22] N.S. Bondareva, B. Buonomo, O. Manca, M.A. Sheremet, Heat transfer performance of the finned nano-enhanced phase change material system under the inclination influence, Int. J. Heat Mass Transf. 135 (2019) 1063–1072.
[23] N. Barhemmati-Rajab, W. Zhao, Investigation into boron nitride nanoparticle effects on thermal properties of calcium chloride hexahydrate ($CaCl_2{\cdot}6H_2O$) as a phase change material, MRS Commun 8 (2018) 1439–1444.
[24] L. Fan, Enhanced thermal conductivity and expedited freezing of nanoparticle suspensions utilized as novel phase change materials, Mechanical Engineering, Auburn University, Auburn, Alabama, 2011.
[25] J. Wang, H. Xie, Z. Xin, Y. Li, L. Chen, Enhancing thermal conductivity of palmitic acid based phase change materials with carbon nanotubes as fillers, Sol. Energy 84 (2010) 339–344.
[26] A.S. Dogonchi, T. Armaghani, A.J. Chamkha, D. Ganji, Natural convection analysis in a cavity with an inclined elliptical heater subject to shape factor of nanoparticles and magnetic field, Arab, J. Sci. Eng. 44 (2019) 7919–7931.

[27] H. Xu, L. Gong, S. Huang, M. Xu, Flow and heat transfer characteristics of nanofluid flowing through metal foams, Int. J. Heat Mass Transf. 83 (2015) 399–407.
[28] T. Tayebi, A.J. Chamkha, Entropy generation analysis during MHD natural convection flow of hybrid nanofluid in a square cavity containing a corrugated conducting block, Int. J. Numer. Method H. 30 (2019) 1115–1136.
[29] M.H. Zahir, S.A. Mohamed, R. Saidur, F.A. Al-Sulaiman, Supercooling of phase-change materials and the techniques used to mitigate the phenomenon, Appl. Energy 240 (2019) 793–817.
[30] Y. Kozak, G. Ziskind, Novel enthalpy method for modeling of PCM melting accompanied by sinking of the solid phase, Int. J. Heat Mass Transf. 112 (2017) 568–586.
[31] Y.M. El Hasadi, Numerical simulation of the melting process of nanostructured based colloidal suspensions phase change materials including the effect of the transport of the particles, J. Mol. Liq. 287 (2019) 110886.
[32] V. Soni, Nanoadditive particles segregation and mobility in phase change materials, Int. J. Heat Mass Transf. 165 (2021) 120676.
[33] C.J. Ho, J.Y. Gao, Preparation and thermophysical properties of nanoparticle-in-paraffin emulsion as phase change material, Int. Commun. Heat Mass Transf. 36 (2009) 467–470.
[34] V. Kumaresan, R. Velraj, S.K. Das, The effect of carbon nanotubes in enhancing the thermal transport properties of PCM during solidification, Heat Mass Transf 48 (2012) 1345–1355.
[35] S. Motahar, N. Nikkam, A.A. Alemrajabi, R. Khodabandeh, M.S. Toprak, M. Muhammed, Experimental investigation on thermal and rheological properties of n-octadecane with dispersed TiO_2 nanoparticles, Int. Commun. Heat Mass Transf. 59 (2014) 68–74.
[36] L.F. Giraldo, B.L. López, L. Pérez, S. Urrego, L. Sierra, M. Mesa, Mesoporous silica applications, Macromolecular Symposia 258 (2007) 129–141.
[37] S. Motahar, N. Nikkam, A.A. Alemrajabi, R. Khodabandeh, M.S. Toprak, M. Muhammed, A novel phase change material containing mesoporous silica nanoparticles for thermal storage: A study on thermal conductivity and viscosity, Int. Commun. Heat Mass Transf. 56 (2014) 114–120.
[38] N. Nikkam, M. Saleemi, M.S. Toprak, S. Li, M. Muhammed, E.B. Haghighi, R. Khodabandeh, B. Palm, Novel nanofluids based on mesoporous silica for enhanced heat transfer, J. Nanopart. Res. 13 (2011) 6201–6206.
[39] S.A.M. Mehryan, M. Vaezi, M. Sheremet, M. Ghalambaz, Melting heat transfer of power-law non-Newtonian phase change nano-enhanced n-octadecane-mesoporous silica ($MPSiO_2$), Int. J. Heat Mass Transf. 151 (2020) 119385.
[40] M. Ghalambaz, S. Mehryan, A. Tahmasebi, A. Hajjar, Non-Newtonian phase-change heat transfer of nano-enhanced octadecane with mesoporous silica particles in a tilted enclosure using a deformed mesh technique, Appl. Math. Model. 85 (2020) 318–337.
[41] M.A. Sheremet, T. Grosan, I. Pop, Free convection in a square cavity filled with a porous medium saturated by nanofluid using Tiwari and Das' nanofluid model, Transp. Porous Media 106 (2015) 595–610.
[42] N.H. Boukani, A. Dadvand, A. Chamkha, Melting of a nano-enhanced phase change material (NePCM) in partially-filled horizontal elliptical capsules with different aspect ratios, Int. J. Mech. Sc. 149 (2018) 164–177.
[43] M. Jahanshahi, S. Hosseinizadeh, M. Alipanah, A. Dehghani, G. Vakilinejad, Numerical simulation of free convection based on experimental measured conductivity in a square cavity using Water/SiO_2 nanofluid, Int. Commun. Heat Mass Transf. 37 (2010) 687–694.
[44] J.N. Reddy, An Introduction to the Finite Element Method, third ed., McGraw-Hill Higher Education, New York, 2006.
[45] R. Kumar, M.A. Kalam, Laminar thermal convection between vertical coaxial isothermal cylinders, Int. J. Heat Mass Transf. 34 (1991) 513–524.
[46] M.H. Matin, W.A. Khan, Laminar natural convection of non-Newtonian power-law fluids between concentric circular cylinders, Int. Commun. Heat Mass Transf. 43 (2013) 112–121.
[47] C. Gau, R. Viskanta, Melting and solidification of a pure metal on a vertical wall, J. Heat Transf. 108 (1986) 174–181.
[48] P. Nithiarasu, K. Seetharamu, T. Sundararajan, Natural convective heat transfer in a fluid saturated variable porosity medium, Int. J. Heat Mass Transf. 40 (1997) 3955–3967.
[49] M. Al-Jethelah, S. Ebadi, K. Venkateshwar, S.H. Tasnim, S. Mahmud, A. Dutta, Charging nanoparticle enhanced bio-based PCM in open cell metallic foams: An experimental investigation, Appl. Therm. Eng. 148 (2019) 1029–1042.
[50] P.T. Sardari, H.I. Mohammed, D. Giddings, G.S. walker, M. Gillott, D. Grant, Numerical study of a multiple-segment metal foam-PCM latent heat storage unit: effect of porosity, pore density and location of heat source, Energy 189 (2019) 116108.
[51] J.M. Mahdi, E.C. Nsofor, Melting enhancement in triplex-tube latent heat energy storage system using nanoparticles-metal foam combination, Appl. Energy 191 (2017) 22–34.
[52] A. Shahsavar, A.A.A.A. Al-Rashed, S. Entezari, P.T. Sardari, Melting and solidification characteristics of a double-pipe latent heat storage system with sinusoidal wavy channels embedded in a porous medium, Energy 171 (2019) 751–769.